RESEARCH ARTICLE

Key Points:
- The role of day-to-night transport in the Martian ionosphere is evaluated
- Transport is dominant within 5300 s after terminator crossing
- A zonal electron flow velocity of 1.9 km/s best reproduces the data

Correspondence to:
J. Cui,
cuij@nao.cas.cn

Day-to-night transport in the Martian ionosphere: Implications from total electron content measurements

J. Cui[1], M. Galand[2], R. V. Yelle[3], Y. Wei[4], and S.-J. Zhang[1,5]

[1]Key Laboratory of Lunar and Deep Space Exploration, National Astronomical Observatories, Chinese Academy of Sciences, Beijing, China, [2]Department of Physics, Imperial College, London, UK, [3]Lunar and Planetary Laboratory, University of Arizona, Tucson, Arizona, USA, [4]Key Laboratory of Earth and Planetary Physics, Institute of Geology and Geophysics, Chinese Academy of Sciences, Beijing, China, [5]Shanghai Astronomical Observatory, Chinese Academy of Sciences, Shanghai, China

Abstract The nightside Martian ionosphere is thought to be contributed by day-to-night transport and electron precipitation, of which the former has not been well studied. In this work, we evaluate the role of day-to-night transport based on the total electron content (TEC) measurements made by the Mars Advanced Radar for Subsurface and Ionospheric Sounding on board Mars Express. This is accomplished by an examination of the variation of nightside TEC in the time domain rather than the traditional solar zenith angle domain. Our analyses here, being constrained to the Northern Hemisphere where the effects of crustal magnetic fields can be neglected, reveal that day-to-night transport serves as the dominant source for the nightside Martian ionosphere from terminator crossing up to time in darkness of $\approx 5.3 \times 10^3$ s, beyond which it is surpassed by electron precipitation. The observations are compared with predictions from a simplified time-dependent ionosphere model. We conclude that the solid body rotation of Mars is insufficient to account for the observed depletion of nightside TEC but the data could be reasonably reproduced by a zonal electron flow velocity of ≈ 1.9 km s^{-1}.

1. Introduction

The dayside Martian ionosphere contains a well-defined primary layer and a low altitude secondary layer that have frequently drawn analogy to the terrestrial F_1 and E layers [*Rishbeth and Mendillo*, 2004]. The former is produced by solar EUV ionization and the latter by solar X-ray ionization along with impact ionization by photoelectrons and their secondaries [e.g., *Fox and Yeager*, 2006]. Existing studies have revealed that both layers vary with solar zenith angle (SZA) and solar ionizing flux as predicted by the idealized Chapman theory [e.g., *Withers*, 2009, and references therein, *Fox and Yeager*, 2009; *Fox and Weber*, 2012]. In contrast, the nightside Martian ionosphere is patchy and sporadic [*Gurnett et al.*, 2008], with impact ionization by precipitating electrons and day-to-night transport generally thought to be the two most important sources [e.g., *Zhang et al.*, 1990].

Investigations of the electron density profiles from the Mars Express (MEx) Radio Science (RS) data have demonstrated that the nightside peak electron density decreases systematically with increasing SZA up to $\approx 115°$, suggesting day-to-night transport as the dominant source [*Withers et al.*, 2012]. Similar conclusions were also made by *Němec et al.* [2010] and *Duru et al.* [2011] based on the MEx Mars Advanced Radar for Subsurface and Ionospheric Sounding (MARSIS) measurements. These authors examined the SZA variation of either the occurrence rate of the nightside ionosphere or the in situ near-terminator electron density at ≈ 200–400 km.

The above data analysis works were accompanied by several modeling efforts that evaluated the importance of day-to-night transport in the Martian ionosphere. In an early investigation, *Fox et al.* [1993] obtained a peak electron density of $\approx 1.3 \times 10^4$ cm^{-3} assuming a nightside downward flux identical to the dayside upward flux derived in *Fox* [1993]. *Ma et al.* [2004] in their multispecies magnetohydrodynamic (MHD) modeling calculated the day-to-night ion transport rate to be $\approx 3 \times 10^{24}$ s^{-1} for high solar activity and $\approx 1 \times 10^{24}$ s^{-1} for low solar activity, driven by pressure gradient and convective electric field under nominal Solar Wind (SW) conditions. More recently, *Chaufray et al.* [2014] made three-dimensional modeling of day-to-night transport in the Martian ionosphere driven by pressure gradient and collisional coupling with

the neutral winds. They calculated the day-to-night ion flow velocity to be $\approx (0.5–1)$ km s^{-1} at an altitude of ≈ 250 km for intermediate solar activity.

Day-to-night transport has been found to be able to support a substantial nightside ionosphere both on Venus [*Knudsen et al.*, 1980; *Spenner et al.*, 1981; *Knudsen and Miller*, 1992] and on Titan [*Cui et al.*, 2009, 2010]. It is the purpose of the present study to investigate in detail the role of such a mechanism on Mars. In section 2, we start with a brief description of the data used for subsequent analyses. This is followed by section 3 where we define a quantity, time in darkness, and examine the variation of the nightside ionosphere in the time domain, to be distinguished from previous investigations in the SZA domain. Two simplified models are then constructed based on the column-integrated continuity equation for thermal electrons, including the solid body rotation model in section 4.1 and the zonal transport model in section 4.2. The latter is used to derive the zonal electron flow velocity required to support the nightside Martian ionosphere. Section 5 is devoted to the comparison with existing results, where we also discuss possible mechanisms driving the day-to-night transport. Finally, we end the paper with discussions and conclusions in section 6.

2. Data Description

Our information on the structure of the nightside Martian ionosphere comes primarily from the radio occultation data acquired by MEx RS and/or the radar sounding data acquired by MEx MARSIS. The former provide the full electron density profiles both above and below the main ionospheric peak [*Pätzold et al.*, 2005]. The latter is available in either the Active Ionospheric Sounding (AIS) mode or the Subsurface (SS) mode [*Picardi et al.*, 2005]. In the AIS mode, the ionospheric echo intensity as a function of time delay and frequency, usually termed as an ionogram, can be used to extract the electron density distribution of the topside ionosphere above the main peak [*Gurnett et al.*, 2005]. In the SS mode, the frequency-dependent phase distortion in the radar signal provides information on the ionospheric TEC, as well as the integrals of higher-order moments of electron distribution, but the detailed electron density profile is unknown [e.g., *Safaeinili et al.*, 2003; *Mouginot et al.*, 2008].

The present study relies exclusively on the MEx MARSIS data obtained in the SS mode. These data, along with the required ephemeris information, are accessible at the Geosciences Node of the NASA Planetary Data System (PDS) Public Archives in tabulated forms. A total number of 1.4 million individual measurements are available from 19 Jun 2005 to 1 Oct 2007 (under solar minimum conditions with a median solar 10.7 cm radio flux index of ≈ 78 at the Earth), of which 0.73 million were obtained at SZA $\gtrsim 90°$. Since our focus here is the global behavior of day-to-night transport, we further exclude all measurements made over the Southern Hemisphere where the presence of strong crustal magnetic fields [e.g., *Acuña et al.*, 1999; *Connerney et al.*, 2001] may complicate the problem by introducing localized features of ionospheric electrodynamics [e.g., *Ulusen and Linscott*, 2008; *Fillingim et al.*, 2010, 2012]. With this, 0.27 million individual measurements are left for subsequent analyses. Both TEC and the second-order moment of electron distribution are used in this work.

3. Variation of the Nightside Ionosphere

3.1. Time in Darkness

To assess the importance of day-to-night transport, previous authors have investigated the SZA variation of the nightside Martian ionosphere [e.g., *Němec et al.*, 2010; *Duru et al.*, 2011; *Withers et al.*, 2012], but this is not a rigorous approach because the observed trend of a diminishing nightside ionosphere with increasing SZA may simply be a geometrical effect in that the Martian ionosphere beyond the terminator is not completely in the shadow with the sunlit portion continuously shrinking as SZA increases. In this study, we switch from the traditional SZA domain to the time domain, by defining a quantity, time in darkness (hereafter TD) as the time elapsed since a given location in the Martian ionosphere crosses the terminator (at SZA $= 90°$). When a given location on Mars rotates progressively to enter the shadow, its SZA and TD increase. However, TD is not a unique function of SZA, and also depends strongly on latitude, LAT.

As an example, we show in Figures 1a–1c the variations of TEC, LAT, and SZA with ephemeris time relative to terminator crossing along the MEx orbit No. 1873. Over the time duration of ≈ 1400 s shown in the figure, MEx moved northward from LAT $\approx 19°$S to $\approx 66°$N and nightward from SZA $\approx 79°$ to $\approx 112°$. Two
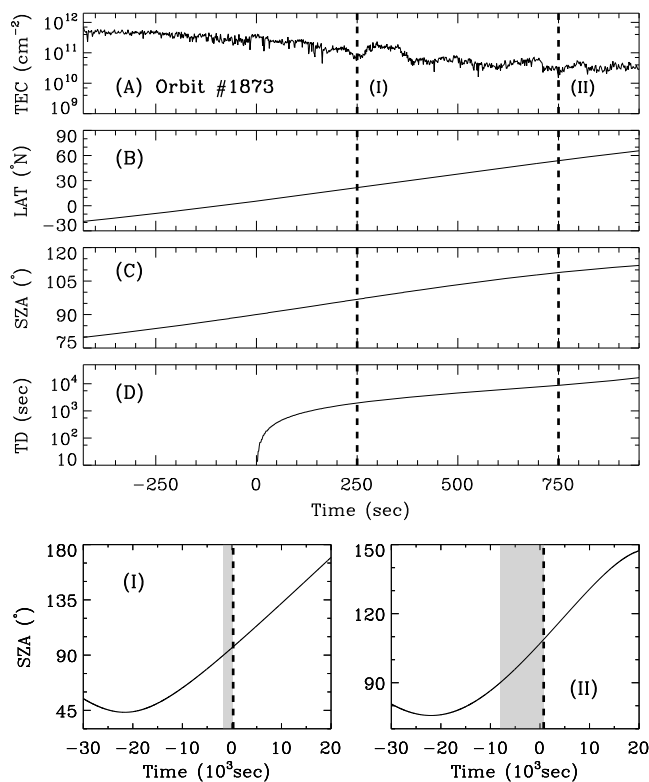
Figure 1. The variations of (a) TEC, (b) LAT, (c) SZA, and (d) time in darkness, TD, with ephemeris time relative to terminator crossing for the MEx orbit No. 1873. Two representative locations are marked by vertical dashed lines and labeled as I and II. The variations of SZA with relative ephemeris time for these locations are shown in the bottom panels. In each panel, TD is given by the width of the shadowed region.
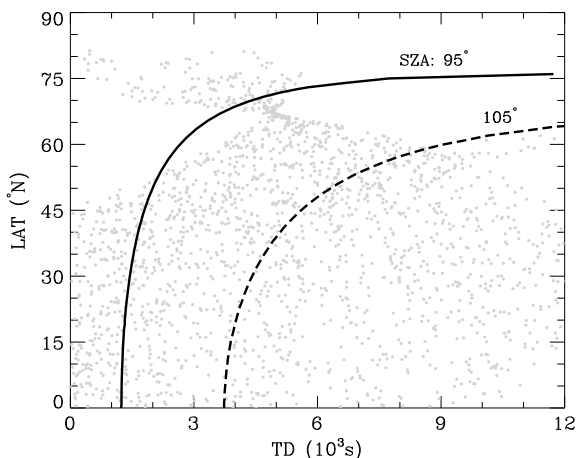

Figure 2. The variations of TD with LAT at SZA = 95° (solid) and SZA = 105° (dashed), respectively, assuming LON = 150°E near 00:48 A.M. on 1 Jan 2007. TD increases with increasing SZA for fixed LAT and increases with increasing LAT for fixed SZA. The grey dots characterize the sample distribution in TD and LAT. To improve visibility, only 2000 randomly chosen measurements are indicated.

representative locations on Mars are marked by vertical dashed lines (labeled as I and II) with LAT $\approx$ 21°N and 54°N. They are intercepted by the MEx orbit at 250 s, 750 s and with SZA of $\approx$ 97°, 109°, respectively.

Following the approach outlined in *Allison* [1997] and *Allison and McEwen* [2000], we calculate the variations of SZA with relative ephemeris time over several full Martian days around the times of orbit interception, for the two representative locations (I) and (II). The results between 3×10^4 s prior to and 2×10^4 s after the times of orbit interception are presented in Figure 1 (bottom). TD corresponds to the time interval between terminator crossing and orbit interception, indicated by the width of the shadowed region in each panel. TD as a function of relative ephemeris time for all individual measurements along the orbit is shown in Figure 1d for reference.

In Figure 2, we show the variations of TD with LAT for several representative choices of SZA, solid for 95° and dashed for 105°. These variations are generated assuming LON = 150°E near 00:48 A.M. on 1 Jan 2007. The dependences of TD on LON and ephemeris time are relatively weak, which are ignored throughout the rest of the paper. TD increases with increasing SZA for fixed LAT and increases with increasing LAT for fixed SZA. The grey dots in Figure 2 characterize the sample distribution in TD and LAT. To improve visibility, only 2000 randomly chosen measurements are indicated. The figure demonstrates that the sample covers a continuous time domain from terminator crossing up to at least TD $\approx 1 \times 10^4$ s only at low latitude and midlatitude. This feature has some impacts on the modeling of day-to-night transport presented in section 4.

3.2. Time Evolution of the Nigthside Ionosphere

We show in Figure 3 the variations of TEC with TD for several selected SZA bins centered at 92.5°, 97.5°,
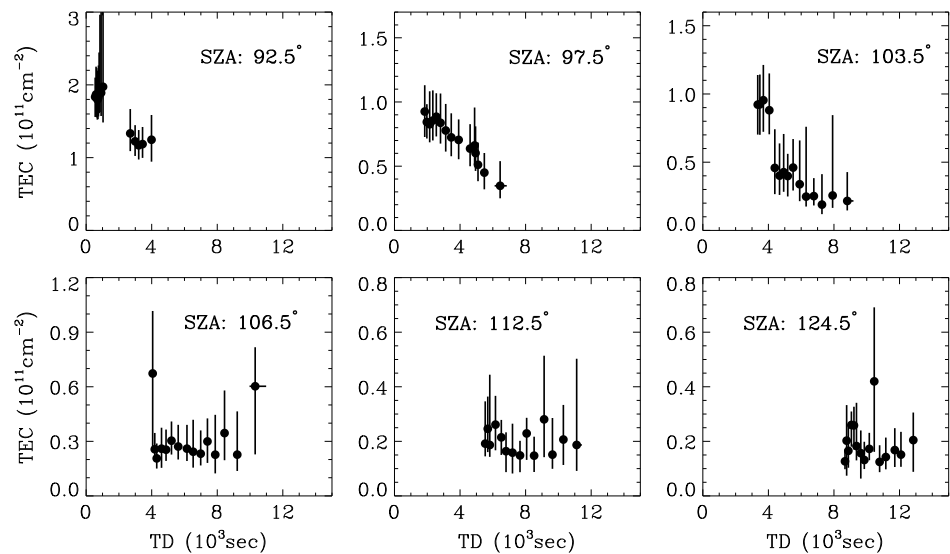
Figure 3. The variations of TEC with TD for several predefined SZA bins centered around 92.5°, 97.5°, 103.5°, 106.5°, 112.5°, and 124.5°, respectively. The bin width is set as 1° such that any SZA variation within the bin is negligible. For each bin, the available TEC measurements are sorted by TD and divided into 15 consecutive TD ranges with equal number of measurements over which the median values of TD and TEC are calculated and shown with the filled circles. The error bars cover the range from 25% to 75% quartiles. Note that the horizontal error bars are usually too small to be observable. (top row) TEC decreases systematically with increasing TD, but such (bottom row) a trend is not obvious.

103.5°, 106.5°, 112.5°, and 124.5°, respectively. The bin width is set as 1° such that any SZA variation within a given bin is negligible. For each bin, the available TEC measurements are sorted by TD and divided into 15 consecutive TD ranges with equal number of measurements over which the median values of TD and TEC are calculated and shown with the filled circles. The error bars cover the range from 25% to 75% quartiles. Figure 3 (top row) reveals a clear trend of decreasing TEC with increasing TD, as indicated by correlation coefficients of ≈ -0.41, -0.46, and -0.48 based on Spearman's ρ test. This is expected by the scenario of day-to-night transport with dayside thermal electrons progressively depleted via recombination as moving into the shadow. In contrast, a similar trend is not seen in Figure 3 (bottom row) for relatively large SZA, with Spearman's ρ correlation coefficients of ≈ 0.02, 0.02, and -0.03, respectively. The absence of any correlation between TD and TEC in these panels implies an alternative nightside source at work, presumably electron precipitation.

It could be shown that the above difference between Figure 3 top and bottom rows is related to the different TD ranges involved, with the former characterized by a TD range reaching as low as $\approx 1 \times 10^3$ s, over which the signature of day-to-night transport is easily seen, and the latter characterized by a significantly higher TD range, over which the signature disappears as most of the dayside thermal electrons have already depleted and the residual amount is surpassed by that produced via in situ electron impact ionization. For further illustration, we show in Figure 4 (top) the Spearman's ρ correlation coefficients between TD and TEC over a large and continuous SZA range with a fixed bin width of 1°. In Figure 4 (bottom), the variation of the corresponding TD range is indicated, with the filled circles giving the median values and the vertical error bars encompassing the 25% and 75% quartiles. The figure shows roughly two regions (labeled by A and B) separated at SZA $\approx 106°$, with a transition in Spearman's ρ correlation coefficient from a median level of ≈ -0.40 for SZA $\lesssim 106°$, characteristic of day-to-night transport, to a median level of ≈ -0.01 for SZA $\gtrsim 106°$, characteristic of electron precipitation. The dividing SZA of 106° corresponds to TD levels that vary with LAT, but a median level of TD $\approx 7 \times 10^3$ s could be obtained based on our sample. We emphasize that previous authors made a similar separation between the two different nightside sources in the SZA domain [e.g., *Němec et al.*, 2010; *Duru et al.*, 2011; *Withers et al.*, 2012], but here the separation is made explicitly in the time domain, which is physically more intuitive. Specifically, we take into full account the variation of TD with both SZA and LAT.
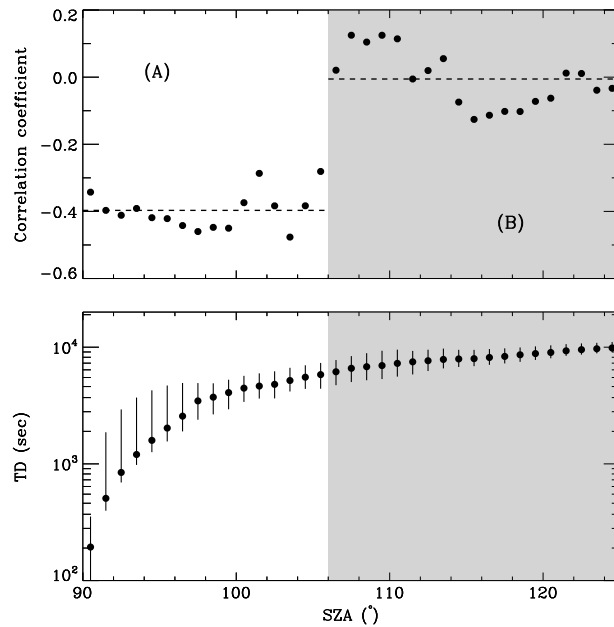
Figure 4. (top) The Spearman's ρ correlation coefficient between TD and TEC as a function of SZA. (bottom) The corresponding TD range is shown, with the solid circles giving the median values and the vertical error bars encompassing the 25% and 75% quartiles. The figure shows roughly two regions (labeled by A and B) separated at SZA $\approx 106°$, with a transition in Spearman's ρ correlation coefficient from a median level of ≈ -0.40 for SZA $\lesssim 106°$, characteristic of day-to-night transport, to a median level of ≈ -0.01 for SZA $\gtrsim 106°$, characteristic of electron precipitation. The median correlation coefficients in both regions are indicated by the horizontal dashed lines.

4. Modeling of the Day-to-Night Transport

We show in section 3 that day-to-night transport helps to maintain a substantial nightside ionosphere within several 10^3s as a given location on Mars passes through the terminator and rotates into the shadow. A natural question is whether the observed depletion of the nightside ionosphere with time can be fully interpreted by the solid body rotation of the planet, and if not, one may further wonder what the required electron flow velocity is.

4.1. Solid Body Rotation Model

The solid body rotation of a planet with a static ionosphere could be considered as the limiting case for day-to-night transport [e.g., *Cui et al.*, 2009]. Ignoring horizontal flow in the noninertial, rotating frame fixed to the solid body surface of Mars, we may write the time evolution of TEC, N_e, as

$$\frac{dN_e}{dt} = P_{ph} + P_{el} - L_{dr}, \qquad (1)$$

where P_{ph} and P_{el} are the column-integrated electron production rates due to solar EUV/X-ray radiation and electron precipitation, respectively, L_{dr} is the column-integrated electron loss rate due to dissociative recombination with O_2^+, the most abundant ion species in the Martian ionosphere [*Hanson et al.*, 1977].

The loss term, L_{dr}, can be written as

$$L_{dr} = \alpha M_e, \qquad (2)$$

where α is the O_2^+ dissociative recombination coefficient, and M_e is the second-order moment of electron number density, n_e, with $M_e = \int_{iono} n_e^2 dr$ (r is the radial coordinate and the integration is over the vertical extent of the entire ionosphere). For the nominal choice, we adopt a constant α of $\approx 2.4 \times 10^{-7}$ cm^3 s^{-1} appropriate for a reference electron temperature of 300 K [*Peverall et al.*, 2001].

Assuming an ideal Chapman profile for the dayside electron distribution [*Withers*, 2009, and references therein], we write the photoionization term, P_{ph}, as

$$P_{ph} = \alpha \frac{M_{e,sub}}{C_h}, \qquad (3)$$

where $M_{e,sub}$ is the subsolar value of M_e and C_h is the Chapman grazing incidence function depending on SZA.

In regions where the effect of photoionization is vanishingly small and where most of the dayside thermal electrons have depleted via recombination, impact ionization by precipitating electrons serves as the only source for the nightside ionosphere with the solution to equation (1) becoming $M_e = P_{el}/\alpha$. Accordingly, the electron precipitation term, P_{el}, could be replaced by

$$P_{el} = \alpha M_{e,prec}, \qquad (4)$$

where $M_{e,prec}$ is the value of M_e contributed by electron precipitation only.
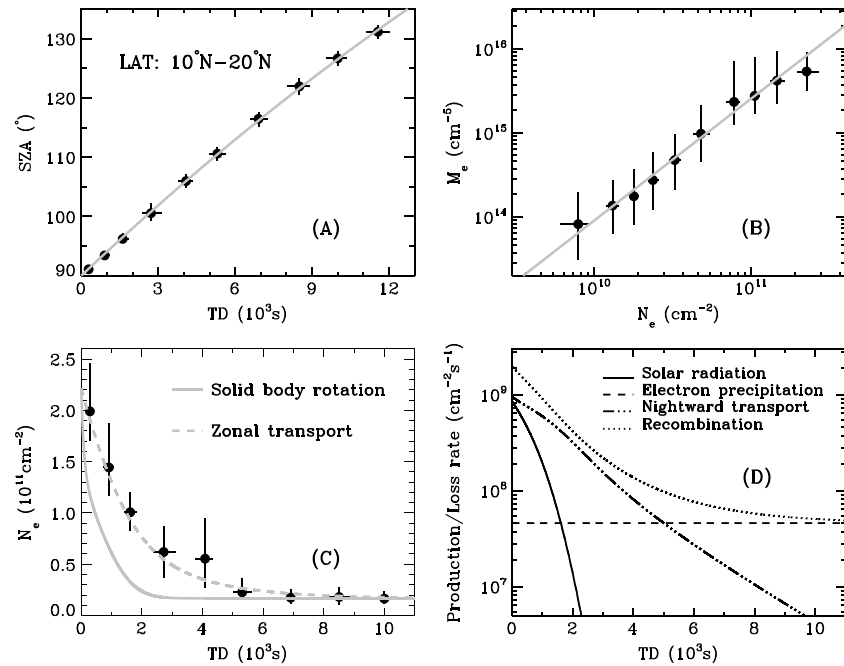
Figure 5. Observations and modeling results for the nightside Martian ionosphere over the meridional band of 10°N–20°N. (a) The variation of SZA with time in darkness, TD, along with the best fit second-order polynomial. (b) The variation of the second-order moment of electron distribution, M_e, with TEC, N_e, along with the best fit power law relation (see equation (6) in the text). (c) The observed time evolution of nightside TEC, with the solid line representing the expected behavior for the solid body rotation model and the dashed line for the best fit zonal transport model assuming a constant zonal electron flow velocity of ≈ 1.9 km s^{-1}. In all these panels, the solid circles give the median values and the error bars encompass the range from 25% to 75% quartiles. (d) The contributions of various production/loss rates as a function of TD, including solar radiation (solid), electron precipitation (dashed), day-to-night transport (dash dotted), and dissociative recombination (dotted), respectively.

Combining the above equations gives

$$\frac{dN_e}{dt} = \alpha \left(\frac{M_{e,\text{sub}}}{C_h} + M_{e,\text{prec}} - M_e \right),$$

(5)

of which the two parameters, $M_{e,\text{sub}}$ and $M_{e,\text{prec}}$, are fully constrained by the data. For $M_{e,\text{sub}}$, we fit the dayside data at SZA $\lesssim 75°$ by $M_e = M_{e,\text{sub}}/C_h$. Unlike the normal Chapman fitting [e.g., *Morgan et al.*, 2008; *Fox and Yeager*, 2009], we exclude the data at $75° \lesssim$ SZA $\lesssim 90°$ to avoid the contribution of day-to-night transport, which is already important there (see below). For $M_{e,\text{prec}}$, we take the median value of all M_e measurements made at SZA $\gtrsim 110°$ (to avoid geometrically partial photoionization) and simultaneously at TD $\gtrsim 8 \times 10^3$ s (to avoid day-to-night transport).

To solve equation (5), the information on the variation of C_h (or equivalently SZA) with TD is required, which scatters considerably in response to the difference in LAT (see Figure 2). Therefore, the model should be applied to a narrow meridional band within which SZA is a monotonic and well-defined function of TD. As an example, we consider the MEx MARSIS measurements made at LAT $\approx 10°$N–20°N. The corresponding relation between SZA and TD is shown in Figure 5a, where the filled circles stand for the median values and the error bars cover the range from 25% to 75% quartiles. The best fit second-order polynomial is given by the solid line for reference.

M_e and N_e are two unknowns in equation (5), thus an extra relation between them is also required. For simplicity, we adopt in this study an empirical relation given by

$$M_e = M_{e,\text{term}} \left(\frac{N_e}{N_{e,\text{term}}} \right)^{\kappa},$$

(6)

where $M_{e,\text{term}}$ and $N_{e,\text{term}}$ are the values of M_e and N_e at SZA = 90° and κ is a power index, all of which are to be constrained by the data. For the meridional band quoted above, these parameters are estimated to be

$\kappa \approx 1.45$, $M_{e,\text{term}} \approx 8.1 \times 10^{15}$ cm^{-5}, and $N_{e,\text{term}} \approx 2.2 \times 10^{11}$ cm^{-2}, respectively, the last of which agrees with the values from *Safaeinili et al.* [2007] and *Lillis et al.* [2010]. The variation of M_e with N_e is shown in Figure 5b, along with the best fit model predicted by equation (6).

With the above approximations, equation (5) is solved numerically based on the fourth-order Runge-Kutta method with the initial condition of $N_e = N_{e,\text{term}} \approx 2.2 \times 10^{11}$ cm^{-2} at $t = 0$ according to our definition of TD. The other parameters required are $M_{e,\text{sub}} \approx 8.3 \times 10^{16}$ cm^{-5} and $M_{e,\text{prec}} \approx 1.9 \times 10^{14}$ cm^{-5}, both determined for the meridional band under consideration. The latter corresponds to a column-integrated electron impact ionization rate of $P_{\text{el}} \approx 4.6 \times 10^{7}$ cm^{-2} s^{-1} (see equation (4)). In Figure 5c, we show the observed time evolution of TEC, with the solid circles representing median values and the error bars encompassing the range from 25% to 75% quartiles. For comparison, the model time evolution predicted by equation (5) is given by the solid line. According to the model, TEC declines to half of its terminator value at TD $\approx 3.4 \times 10^{2}$ s (hereafter referred to as depletion time constant), whereas the observation exhibits a much longer depletion time constant of $\approx 1.3 \times 10^{3}$ s. Clearly, solid body rotation is insufficient to account for the observation and a considerable day-to-night flow in the noninertial, rotating frame of Mars is required.

It is instructive to evaluate how the choice of the O_2^+ dissociative recombination coefficient would affect the model time evolution. The dashed line in Figure 5c corresponds to the solid body rotation model with an imaginary recombination coefficient of $\approx 2.6 \times 10^{-8}$ cm^3 s^{-1} which is a factor of ≈ 8 lower than our nominal choice represented by the solid line in the same panel. Interestingly, such a model agrees well with the observed depletion of nightside TEC. All existing measurements of the O_2^+ dissociative recombination coefficient, α, at 300 K agree within 15% [*McLain et al.*, 2004]. Meanwhile, since α is proportional to electron temperature to the power of -0.7 [*Peverall et al.*, 2001; *McLain et al.*, 2004], the reduced value of α reported above would then imply an exceptionally high electron temperature of $\approx 7.2 \times 10^{3}$ K, which, at ionospheric altitudes, is not predicted by any existing models [e.g., *Matta et al.*, 2014; *Withers et al.*, 2014]. Strictly speaking, α in equation (2) refers to the O_2^+ dissociative recombination coefficient weighted by electron density squared. Therefore, even if very high electron temperatures (and thus very low recombination coefficients) could be reached well above the ionospheric peak due to the sharp increase in electron temperature with increasing altitude [*Hanson and Mantas*, 1988], they should not have an appreciable influence on our model solution obtained with the nominal choice of $\alpha \approx 2.4 \times 10^{-7}$ cm^3 s^{-1}. For instance, assuming an asymptotic topside electron temperature of $\approx 3 \times 10^{3}$ K [*Hanson and Mantas*, 1988] and using the empirical electron density profile of *Němec et al.* [2011] in the diffusion region, it could be estimated that the contribution of α above 200 km is no more than 2%. This is appropriate for SZA $\approx 44°$ where the only measurement of electron temperature in the Martian ionosphere is available, but we expect a quantitatively similar result for near-terminator conditions as well. The above discussions indicate that the disagreement in the depletion time constant cannot be reconciled by the uncertainty in the O_2^+ dissociative recombination coefficient. However, we show below that it could be favorably interpreted by an imposed day-to-night electron flow velocity.

4.2. Zonal Transport Model

We now generalize the solid body rotation model to a model also including electron transport. When column integrated over the entire ionosphere, the advection term of the continuity equation for thermal electron density becomes

$$\int_{\text{iono}} \left[\frac{\partial(n_e V_r)}{\partial r} + \frac{1}{r} \frac{\partial(n_e V_\theta)}{\partial \theta} + \frac{1}{r \cos\theta} \frac{\partial(n_e V_\phi)}{\partial \phi} \right] dr \approx \frac{V_\phi}{R_M \cos\theta} \frac{\partial N_e}{\partial \phi}, \tag{7}$$

where θ and ϕ represent LAT and LON, V_r, V_θ, and V_ϕ are the radial, meridional, and zonal components of the electron flow velocity, R_M is the mean Mars radius, and other quantities have been defined above. Several assumptions are implicitly used in reaching equation (7). First, the slabness of the Martian ionosphere is small compared to the mean Mars radius [e.g., *Lillis and Brain*, 2013] and therefore r is fixed with $r = R_M \approx 3390$ km. Second, the zonal flow is characterized by a constant velocity, V_ϕ, at ionospheric altitudes, whereas the meridional electron flow is ignored for simplicity. Third, we assume no electron outflow at the top of the Martian ionosphere and therefore the integral involving V_r on the left hand side of equation (7) disappears.

Table 1. The Subsolar TEC, $N_{e,\text{sub}}$, the Near-Terminator TEC , $N_{e,\text{term}}$, and the TEC in the Deep Nightside Ionosphere Contributed by Electron Precipitation Only, $N_{e,\text{prec}}$, for Different Meridional Bands on Mars[a]

LAT	$N_{e,\text{sub}}$ (cm^{-2})	$N_{e,\text{term}}$ (cm^{-2})	$N_{e,\text{prec}}$ (cm^{-2})	τ_{SB} (s)	τ_{trans} (s)	$\alpha/\alpha_{\text{eff}}$	V_ϕ (km s^{-1})	τ_{eq} (s)
0°N–10°N	9.3×10^{11}	2.2×10^{11}	2.0×10^{10}	4.7×10^2	1.4×10^3	8.7	1.9	4.8×10^3
10°N–20°N	9.2×10^{11}	2.2×10^{11}	1.8×10^{10}	3.4×10^2	1.3×10^3	9.3	2.0	5.0×10^3
20°N–30°N	9.1×10^{11}	2.7×10^{11}	1.7×10^{10}	2.0×10^2	1.1×10^3	9.4	1.9	5.3×10^3
30°N–40°N	8.1×10^{11}	2.5×10^{11}	1.5×10^{10}	1.8×10^2	1.2×10^3	10	1.9	5.6×10^3
40°N–50°N	9.5×10^{11}	2.5×10^{11}	1.6×10^{10}	4.1×10^2	1.7×10^3	12	1.9	6.6×10^3
Median	9.2×10^{11}	2.5×10^{11}	1.7×10^{10}	3.4×10^2	1.3×10^3	9.4	1.9	5.3×10^3
Uncertainty	5.4×10^{10}	2.1×10^{10}	2.0×10^9	1.3×10^2	2.2×10^2	1.3	0.04	6.9×10^2

[a]Also listed are the depletion time constants for both the solid body rotation model, τ_{SB}, and the best fit zonal transport model, τ_{trans}, the ratio of the nominal recombination coefficient, α, to the effective recombination coefficient, α_{eff}, the best fit zonal electron flow velocity, V_ϕ, and the time interval from terminator crossing to when the effects of transport and electron precipitation are equal, τ_{eq}. The median values and the uncertainties are provided in the bottom two lines for reference.

With equation (7), the column-integrated continuity equation for thermal electrons becomes

$$\frac{dN_e}{dt} = \alpha \left(\frac{M_{e,\text{sub}}}{C_h} + M_{e,\text{prec}} - M_e \right) - \frac{V_\phi}{R_M \cos\theta} \frac{dN_e}{d\phi}, \tag{8}$$

or equivalently,

$$\left(1 + \frac{V_\phi}{V_M \cos\theta} \right) \frac{dN_e}{dt} = \alpha \left(\frac{M_{e,\text{sub}}}{C_h} + M_{e,\text{prec}} - M_e \right), \tag{9}$$

where $V_M \approx 0.24$ km s^{-1} is the solid body rotational velocity of Mars at the equator. This implies that an effective dissociative recombination coefficient, α_{eff}, could be defined in terms of the nominal dissociative recombination coefficient, α, given by

$$\alpha_{\text{eff}} = \frac{\alpha}{1 + V_\phi/(V_M \cos\theta)}, \tag{10}$$

from which a best fit value of $\alpha_{\text{eff}} \approx 2.6 \times 10^{-8}$ cm^3 s^{-1} implied by Figure 5 leads to a zonal electron flow velocity of $V_\phi \approx 2.0$ km s^{-1}.

For the best fit model given by the dashed line in Figure 5c, it is interesting to compare the contributions of different production/loss terms in the balance of nightside TEC on Mars. This is illustrated in Figure 5d of the same figure where various column-integrated production/loss rates are plotted as a function of TD. Note that the sum of all production rates is not identical to the loss rate because the nightside ionosphere is not in a steady state. Near the terminator, the electron impact ionization rate accounts for only $\approx 5\%$ of the photoionization rate, whereas the effect of transport is comparable to the effect of solar radiation according to our calculations. The latter also explains why the best fit values of $N_{e,\text{sub}}$ and $M_{e,\text{sub}}$ are derived in this work from the dayside measurements made at SZA $\lesssim 75°$ (see above). Day-to-night transport is the dominant plasma source maintaining the nightside Martian ionosphere throughout the TD range of TD $\lesssim 5.0 \times 10^3$ s (corresponding to SZA $\lesssim 109°$ for the meridional band under consideration), beyond which electron precipitation becomes more important.

The approach described above could be easily repeated for other meridional bands. Figure 2 demonstrates that at high northern latitudes, the sampling of the nightside Martian ionosphere does not cover the TD range critical for characterizing transport. Therefore, to be conservative, our modeling efforts are restricted to the regions southward of 50°N. We consider five consecutive meridional bands with a fixed band width of 10° in LAT. We list in Table 1 the respective values of subsolar TEC, $N_{e,\text{sub}}$, near-terminator TEC, $N_{e,\text{term}}$, and deep nightside TEC contributed by electron precipitation only, $N_{e,\text{prec}}$. Also tabulated are the depletion time constants for both the solid body rotation model, τ_{SB}, and the best fit zonal transport model, τ_{trans}, the ratio of the nominal recombination coefficient to the effective recombination coefficient, $\alpha/\alpha_{\text{eff}}$, the best fit zonal
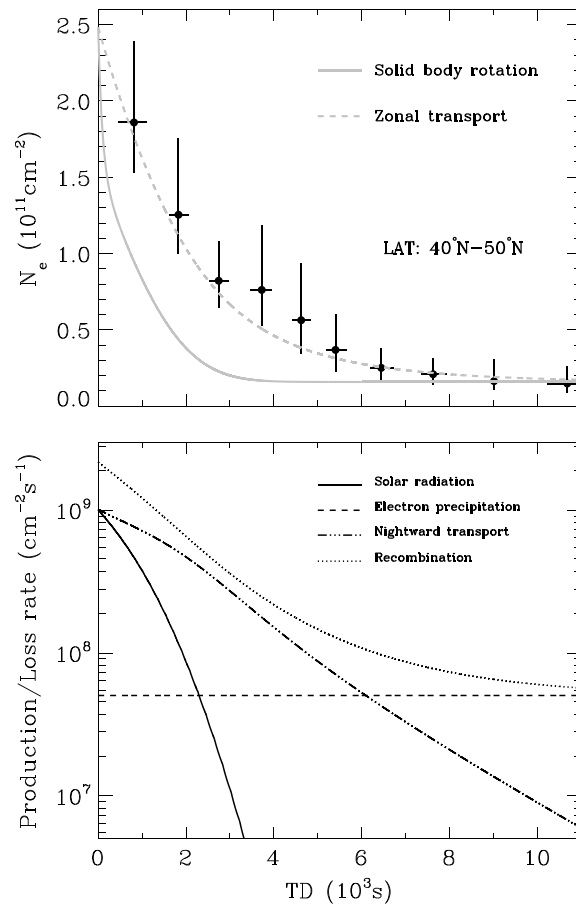
Figure 6. Similar to Figure 5 but for the meridional band of 50°N–60°N. Only the observed/modeled time evolution of night-side TEC and the contributions of various production/loss terms to the nightside TEC balance are shown.

electron flow velocity, V_ϕ, and the time interval from terminator crossing to when the effects of transport and electron precipitation are equal, τ_{eq}. The median values and the uncertainties (determined from the standard deviations among different cases) are given in the bottom two lines for reference.

All the characteristics of the nightside Martian ionosphere described so far are confirmed by the modeling results for the range of meridional bands covered in Table 1. For example, the observed/modeled time evolution of nightside TEC is shown in Figure 6 for the meridional band of $\approx 40°N–50°N$, where we also compare the contributions of various production/loss terms to the nightside TEC balance. Again, the solid body rotation model predicts a depletion time constant of $\approx 4.1 \times 10^2$ s, which is far insufficient to account for the observed depletion with a time constant of $\approx 1.7 \times 10^3$ s. The effect of day-to-night transport is nearly identical to that of photoionization at the terminator, but the former declines more slowly than the latter as moving progressively into the shadow. At $TD \gtrsim 6.6 \times 10^3$ s, transport is surpassed by electron precipitation.

Table 1 reveals that the ratio, α/α_{eff}, increases systematically northward from the equator. However, such a trend is nearly exactly compensated for by the decline in $\cos\theta$ with increasing LAT, leading to a remarkably constant level of zonal electron flow velocity at ≈ 1.9 km s^{-1} with a very small scattering of $\approx 2\%$. This means that day-to-night transport in the Martian ionosphere occurs in a fairly uniform pattern, at least for low and middle northern latitudes. Another interesting feature revealed by Table 1 is an equatorward decrease in τ_{eq}, but based on an inspection of the simultaneous variation in $N_{e,prec}$, this simply reflects an enhanced level of electron precipitation near the equator rather than an intrinsic feature of day-to-night transport. The meridional variation in electron precipitation is beyond the scope of the present study and will not be further scrutinized here. It remains to be seen if such a variation is related to different SW dynamic pressure and/or different interplanetary magnetic field clock angle sampled at different meridional bands [e.g., *Crider et al.*, 2003; *Brain et al.*, 2007; *Lillis and Brain*, 2013].

We may further convert the zonal electron flow velocity, V_ϕ, to a characteristic day-to-night electron transport rate through

$$\int_{R_M}^{+\infty} \int_{-\pi/2}^{\pi/2} n_{e,term}(r)V_\phi r \, d\theta \, dr \approx \frac{\pi}{2} R_M V_\phi N_{e,term}, \quad (11)$$

where $n_{e,term}(r)$ is the electron number density as a function of radial coordinate, r, near the terminator. With $N_{e,term} \approx 2.5 \times 10^{11}$ cm^{-2}, $V_\phi \approx 1.9$ km s^{-1} from Table 1 and assuming that these values are meridionally constant, equation (11) leads to an electron transport rate of $\approx 2.6 \times 10^{25}$ s^{-1}. However, this value might be overestimated if we take into account the influences of the strong crustal magnetic fields preferentially located over the Southern Hemisphere [e.g., *Ma et al.*, 2002].

5. Comparison With Existing Results and Implications

The characteristic zonal electron flow velocity derived here represents some sort of average velocity necessary for maintaining the observed nightside TEC on Mars. It applies to cold ionospheric electrons with energies typically below 1 eV, to be distinguished from suprathermal electrons that have been measured extensively by in situ particle instruments, such as the Electron Reflectometer on board Mars Global Surveyor [e.g., *Ulusen and Linscott*, 2008] and the Analyzer of Space Plasmas and Energetic Atoms 3 (ASPERA-3) Electron Spectrometer on board MEx [e.g., *Frahm et al.*, 2010]. However, it is possible to compare our derived electron flow velocity to measurements of cold ionospheric ions on Mars, since charge neutrality implies that ionospheric electrons and ions have comparable flow velocities. It is also instructive to compare this study to some previous modeling works that incorporated the effects of day-to-night transport.

An early modeling effort for day-to-night transport was presented by *Fox et al.* [1993], which is different from ours in at least two aspects. First, *Fox et al.* [1993] adopted a more sophisticated chemical scheme which allowed them to predict the nightside contents of not only thermal electrons but also various ion species. In contrast, we use a scheme that ignores ion-neutral reactions and treats O_2^+ dissociative recombination as the only loss mechanism for thermal electrons. Such a simplified scheme has been widely accepted in previous simulation works [e.g., *Fillingim et al.*, 2007; *Lillis et al.*, 2009] and has been found to be able to reproduce well the general features of the Martian ionosphere, thanks to the dominance of O_2^+ near the ionospheric peak [*Hanson et al.*, 1977]. Second, the model of *Fox et al.* [1993] is essentially a steady state one, with the effects of transport simulated by imposing a downward flow at the top of the nightside ionosphere. This places strict constraints on the pattern of day-to-night transport through horizontal flow on planet-wide scale ascending above the ionopause at the dayside and descending below at the nightside, which is not necessarily realistic as motivated by our understanding of day-to-night transport on other planets [e.g., *Knudsen et al.*, 1980; *Spenner et al.*, 1981; *Knudsen and Miller*, 1992; *Cui et al.*, 2009, 2010]. In contrast, here we solve explicitly the time evolution of the Martian ionosphere from terminator crossing to the deep nightside with the nightward flow occurring zonally below the ionopause. To capture the essential features of day-to-night transport, a chemically simplified but time-dependent scheme seems more realistic than a chemically robust but steady state scheme.

Withers et al. [2012] derived a day-to-night electron flow velocity of ≈ 2 km s^{-1} based on two specific nightside electron density profiles at SZA $\approx 104°$ for low solar activity (see A4 and A5 in their Figure 3). This is in perfect agreement with our value, despite that their two profiles were obtained at 76°N to be distinguished from our case appropriate for low latitude and midlatitude. Such an agreement results from a common rationale that constrains the electron flow velocity with the observed depletion time constant.

Recently, *González-Galindo et al.* [2013] and *Chaufray et al.* [2014] presented detailed modelings of the three-dimensional structure of the Martian ionosphere, at both the dayside and the nightside, by coupling a simplified Martian ionosphere model to a Martian global circulation model extending from the surface up to the exobase [e.g., *Angelats i Coll et al.*, 2005; *González-Galindo et al.*, 2009a, 2009b]. These two works are different in that the former assumes diffusive equilibrium for all species under consideration whereas the latter includes the effects of transport, both vertically and horizontally. Therefore, the solid body rotation model presented in section 4.1 is comparable to the *González-Galindo et al.* [2013] model, and the zonal transport model in section 4.2 serves as one particular case of the *Chaufray et al.* [2014] model that ignores meridional flow. All works reflect properly the expected situation of a quick depletion of the ionospheric content as passing across the terminator in the case of solid body rotation only and a delayed depletion in the case of strong nightward transport [see *Chaufray et al.*, 2014, Figure 8]. *Chaufray et al.* [2014] derived a characteristic day-to-night flow velocity of several 10^2 m s^{-1} for both ions and electrons, which is significantly lower than the value of ≈ 1.9 km s^{-1} reported in section 4.2.

The above discrepancy is related to the key difference between our zonal transport model and the *Chaufray et al.* [2014] model, in that the former constrains the flow velocity from the data, whereas the latter from a prescribed local momentum budget. Specifically, *Chaufray et al.* [2014] considered an ionospheric plasma flow driven by collisional coupling to the neutral winds and diurnal pressure gradient. Such a scheme is not able to reproduce the observed depletion of nightside TEC on Mars, indicating that an important mechanism is missing in their model, presumably momentum transfer from the SW [e.g., *Pérez-de-Tejada*, 1998; *Pérez-de-Tejada et al.*, 2013]. However, the MHD calculations of *Ma et al.* [2004], which did take into

account both pressure gradient and momentum transfer via the SW convective electric fields, predicted a day-to-night transport rate of only several 10^{24} s^{-1}, about an order of magnitude lower than our result. It remains to be seen if some other processes of momentum transfer from the SW, such as the wave particle interactions [*Ergun et al.*, 2006], can explain the large day-to-night electron flow velocity obtained in the present study.

While direct measurements of the cold ionospheric electron flow are not available, transterminator flow velocities of cold ions have been obtained with the ASPERA-3 ion mass analyzer (IMA) measurements made on board MEx. Early IMA investigations covered the ion energy range above 30 eV [e.g., *Barabash et al.*, 2007; *Lundin et al.*, 2008a], not representative of cold ionospheric ions. A new patch uploaded on 1 May 2007 improved the IMA performance and extended the energy range to cover cold ionospheric ions with energies below 10 eV [e.g., *Lundin et al.*, 2008b; *Fränz et al.*, 2010]. Specifically, *Fränz et al.* [2010] obtained a transterminator ion velocity of ≈ 5 km s^{-1} for both O$^+$ and O$_2^+$ under solar minimum conditions.

We caution that the transterminator flow in our work is exclusively associated with day-to-night transport (since escape is ignored in equation (9)), whereas that of *Fränz et al.* [2010] represents a combination of day-to-night transport and escape. For example, the MHD modeling results of *Ma et al.* [2002, 2004] showed that the contributions of the two processes to the transterminator ion flow were comparable. In addition, the electron flow velocity in equation (7) is weighted by the vertical electron density profile, thus is mainly representative of the altitude range of 80–170 km where the nightside electron density peak is located [*Zhang et al.*, 1990; *Withers et al.*, 2012]. In contrast, the *Fränz et al.* [2010] results apply to altitudes above 300 km. Such a distinction should be born in mind since electron/ion dynamics may vary substantially with altitude [*Miller and Whitten*, 1991]. Despite the above difficulties in a direct comparison between the two works, both appear to suggest a common scenario in which cold ionospheric ions and electrons are accelerated to velocities reaching several km s^{-1}, sufficient to maintain a substantial nightside ionosphere on Mars. Given that the plasma sound velocity in the Martian ionosphere is below 1 km s^{-1}, the nightward flow is supersonic.

6. Discussions and Concluding Remarks

A substantial ionosphere at the nightside of Mars is generally thought to be contributed by day-to-night transport or electron precipitation [e.g., *Zhang et al.*, 1990], of which the former has been studied less in depth in previous works, both observationally and theoretically.

Here based on the MEx MARSIS measurements made in the SS mode, we examine the variation of the nightside Martian ionosphere in the time domain, through a parameter, time in darkness (TD), defined as the time elapsed since a given location in the Martian ionosphere passes through the terminator. Such an approach is to be distinguished from previous investigations of day-to-night transport in the SZA domain [e.g., *Němec et al.*, 2010; *Duru et al.*, 2011; *Withers et al.*, 2012]. Being constrained to the data from the Northern Hemisphere only that are supposed to be unaffected by strong crustal magnetic fields [e.g., *Acuña et al.*, 1999; *Connerney et al.*, 2001], our analyses reveal that the nightside TEC decreases systematically with increasing TD up to several 10^3 s, indicative of day-to-night transport; and that at larger TD, it flattens off to a near constant level, indicative of electron precipitation.

A simplified model is constructed based on the column-integrated continuity equation for thermal electrons and applied to the data at low and middle northern latitudes for both the solid body rotation case and the zonal transport case. Data-model comparison suggests that the solid body rotation of Mars predicts a depletion time constant of only $\approx 3.4 \times 10^2$ s, significantly shorter than the actual depletion time constant of $\approx 1.3 \times 10^3$ s, where the depletion time constant is defined as the time interval from terminator crossing up to when the nightside TEC declines by a factor of 2. However, the data could be reasonably reproduced by imposing a constant zonal electron flow velocity of ≈ 1.9 km s^{-1}. The contributions from various production terms in the balance of nightside TEC are also evaluated, from which we conclude that (1) the effect of day-to-night transport is comparable to that of solar EUV/X-ray radiation already near the terminator, and (2) transport serves as the dominant source for the nightside ionosphere from terminator crossing up to TD $\approx 5.3 \times 10^3$ s, beyond which it is surpassed by electron precipitation. It is noteworthy that the presence/absence of an anticorrelation between TEC and TD, as demonstrated by Figure 4 in section 3.1, predicts a similar TD level separating the two sources that maintain the nightside ionosphere.

The zonal electron flow velocity of ≈ 1.9 km s^{-1} derived in this work agrees with the crude estimate of *Withers et al.* [2012], despite that the data sets from the two studies were obtained at different latitudes. Comparison to the recent three-dimensional modeling results of *Chaufray et al.* [2014] suggests that our derived zonal electron flow velocity is significantly higher than their value, typically several 10^2 m s^{-1}. However, we note that our value is directly constrained by the data, and theirs is obtained with a designated budget of momentum balance in the Martian ionosphere.

Although we show undoubtedly that day-to-night transport serves as an important source for the nightside Martian ionosphere, it is unclear what the main force driving the supersonic plasma flow is. Diurnal pressure gradient does not provide a solution [e.g., *Chaufray et al.*, 2014], and it remains to be evaluated if momentum transfer from the SW is sufficient [e.g., *Ma et al.*, 2004]. Here some insights could be gained by comparing our case with the supersonic transterminator ion flow on Venus [e.g., *Knudsen et al.*, 1980]. It is known that the pressure gradient force can only drive ionospheric ions to supersonic conditions through a nozzle-like configuration, but such a situation is not easily provided at Mars [*Pérez-de-Tejada*, 1986a; *Whitten et al.*, 1991; *Pérez-de-Tejada et al.*, 1993]. Meanwhile, the pressure gradient force model fails to predict the dawn-dusk asymmetry in the observed ion flow pattern [*Pérez-de-Tejada*, 1986b; *Miller and Whitten*, 1991; *Pérez-de-Tejada*, 2008]. Instead, it is generally thought that momentum transfer from the SW plays an important role in supporting the supersonic ionospheric flow on Venus. [e.g., *Pérez-de-Tejada*, 1998; *Pérez-de-Tejada et al.*, 2013].

The zonal transport model presented in section 4.2 provides only one solution capable of reproducing the observed depletion of nightside TEC. It is not known a priori whether meridional transport could indeed be neglected. It is also interesting to examine how the derived flow velocities would be affected if an upper boundary condition is imposed characterizing escape, especially for applications to solar maximum conditions [*Lundin et al.*, 2008a]. In addition, our main focus here is day-to-night transport over the Northern Hemisphere with a magnetic field topology of a typical induced magnetosphere [*Brain*, 2006, 2010], but the role of such a mechanism over the Southern Hemisphere might be different. For example, *Ma et al.* [2002] predicted the day-to-night flow to be reduced by more than 30% with crustal magnetic fields incorporated in their MHD modeling.

References

Acuña, M. H., et al. (1999), Global distribution of crustal magnetization discovered by the Mars Global Surveyor MAG/ER experiment, *Science*, *284*, 790–793, doi:10.1126/science.284.5415.790.

Allison, M. (1997), Accurate analytic representations of solar time and seasons on Mars with applications to the Pathfinder/Surveyor missions, *Geophys. Res. Lett.*, *24*, 1967–1970, doi:10.1029/97GL01950.

Allison, M., and M. McEwen (2000), A post-Pathfinder evaluation of areocentric solar coordinates with improved timing recipes for Mars seasonal/diurnal climate studies, *Planet. Space Sci.*, *48*, 215–235, doi:10.1016/S0032-0633(99)00092-6.

Angelats i Coll, M., F. Forget, M. A. López-Valverde, and F. González-Galindo (2005), The first Mars thermospheric general circulation model: The Martian atmosphere from the ground to 240 km, *Geophys. Res. Lett.*, *32*, L04201, doi:10.1029/2004GL021368.

Barabash, S., et al. (2007), The loss of ions from Venus through the plasma wake, *Nature*, *450*, 650–653, doi:10.1038/nature06434.

Brain, D. A. (2006), Mars global surveyor measurements of the Martian solar wind interaction, *Space Sci. Rev.*, *126*, 77–112, doi:10.1007/s11214-006-9122-x.

Brain, D. A., R. J. Lillis, D. L. Mitchell, J. S. Halekas, and R. P. Lin (2007), Electron pitch angle distributions as indicators of magnetic field topology near Mars, *J. Geophys. Res.*, *112*, A09201, doi:10.1029/2007JA012435.

Brain, D. A., et al. (2010), A comparison of global models for the solar wind interaction with Mars, *Icarus*, *206*, 139–151, doi:10.1016/j.icarus.2009.06.030.

Chaufray, J.-Y., F. Gonzalez-Galindo, F. Forget, M. Lopez-Valverde, F. Leblanc, R. Modolo, S. Hess, M. Yagi, P.-L. Blelly, and O. Witasse (2014), Three-dimensional Martian ionosphere model: II. Effect of transport processes due to pressure gradients, *J. Geophys. Res. Planets*, *119*, 1614–1636, doi:10.1002/2013JE004551.

Connerney, J. E. P., M. H. Acuña, P. J. Wasilewski, G. Kletetschka, N. F. Ness, H. Rème, R. P. Lin, and D. L. Mitchell (2001), The global magnetic field of Mars and implications for crustal evolution, *Geophys. Res. Let.*, *28*, 4015–4018, doi:10.1029/2001GL013619.

Crider, D. H., D. Vignes, A. M. Krymskii, T. K. Breus, N. F. Ness, D. L. Mitchell, J. A. Slavin, and M. H. Acuña (2003), A proxy for determining solar wind dynamic pressure at Mars using Mars global surveyor data, *J. Geophys. Res.*, *108*(A12), 1461, doi:10.1029/2003JA009875.

Cui, J., M. Galand, R. V. Yelle, V. Vuitton, J.-E. Wahlund, P. P. Lavvas, I. C. F. Müller-Wodarg, T. E. Cravens, W. T. Kasprzak, and J. H. Waite Jr. (2009), Diurnal variations of Titan's ionosphere, *J. Geophys. Res.*, *114*, A06310, doi:10.1029/2009JA014228.

Cui, J., M. Galand, R. V. Yelle, J.-E. Wahlund, K. Ågren, J. H. Waite Jr., and M. K. Dougherty (2010), Ion transport in Titan's upper atmosphere, *J. Geophys. Res.*, *115*, A06314, doi:10.1029/2009JA014563.

Duru, F., D. A. Gurnett, D. D. Morgan, J. D. Winningham, R. A. Frahm, and A. F. Nagy (2011), Nightside ionosphere of Mars studied with local electron densities: A general overview and electron density depressions, *J. Geophys. Res.*, *116*, A10316, doi:10.1029/2011JA016835.

Ergun, R. E., L. Andersson, W. K. Peterson, D. Brain, G. T. Delory, D. L. Mitchell, R. P. Lin, and A. W. Yau (2006), Role of plasma waves in Mars' atmospheric loss, *J. Geophys. Res.*, *33*, L14103, doi:10.1029/2006GL025785.

Fillingim, M. O., L. M. Peticolas, R. J. Lillis, D. A. Brain, J. S. Halekas, D. L. Mitchell, R. P. Lin, D. Lummerzheim, S. W. Bougher, and D. L. Kirchner (2007), Model calculations of electron precipitation induced ionization patches on the nightside of Mars, *Geophys. Res. Lett.*, *34*, L12101, doi:10.1029/2007GL029986.

Fillingim, M. O., L. M. Peticolas, R. J. Lillis, D. A. Brain, J. S. Halekas, D. Lummerzheim, and S. W. Bougher (2010), Localized ionization patches in the nighttime ionosphere of Mars and their electrodynamic consequences, *Icarus*, *206*, 112–119, doi:10.1016/j.icarus.2009.03.005.

Fillingim, M. O., R. J. Lillis, S. L. England, L. M. Peticolas, D. A. Brain, J. S. Halekas, C. Paty, D. Lummerzheim, and S. W. Bougher (2012), On wind-driven electrojets at magnetic cusps in the nightside ionosphere of Mars, *Earth Planets Space*, *64*, 93–103, doi:10.5047/eps.2011.04.010.

Fox, J. L. (1993), On the escape of oxygen and hydrogen from Mars, *Geophys. Res. Lett.*, *20*, 1747–1750, doi:10.1029/93GL01118.

Fox, J. L., and K. E. Yeager (2006), Morphology of the near-terminator Martian ionosphere: A comparison of models and data, *J. Geophys. Res.*, *111*, A10309, doi:10.1029/2006JA011697.

Fox, J. L., and K. E. Yeager (2009), MGS electron density profiles: Analysis of the peak magnitudes, *Icarus*, *200*, 468–479, doi:10.1016/j.icarus.2008.12.002.

Fox, J. L., and A. J. Weber (2012), MGS electron density profiles: Analysis and modeling of peak altitudes, *Icarus*, *221*, 1002–1019, doi:10.1016/j.icarus.2012.10.002.

Fox, J. L., J. F. Brannon, and H. S. Porter (1993), Upper limits to the nightside ionosphere of Mars, *Geophys. Res. Lett.*, *20*, 1339–1342, doi:10.1029/93GL01349.

Frahm, R. A., et al. (2010), Estimation of the escape of photoelectrons from Mars in 2004 liberated by the ionization of carbon dioxide and atomic oxygen, *Icarus*, *206*, 50–63, doi:10.1016/j.icarus.2009.03.024.

Fränz, M., E. Dubinin, E. Nielsen, J. Woch, S. Barabash, R. Lundin, and A. Fedorov (2010), Transterminator ion flow in the Martian ionosphere, Planet, *Space Sci.*, *58*, 1442–1454, doi:10.1016/j.pss.2010.06.009.

González-Galindo, F., F. Forget, M. A. López-Valverde, M. Angelats i Coll, and E. Millour (2009a), A ground-to-exosphere Martian general circulation model: 1. Seasonal, diurnal, and solar cycle variation of thermospheric temperatures, *J. Geophys. Res.*, *114*, E04001, doi:10.1029/2008JE003246.

González-Galindo, F., F. Forget, M. A. López-Valverde, and M. Angelats i Coll (2009b), A ground-to-exosphere Martian general circulation model: 2. Atmosphere during solstice conditions—Thermospheric polar warming, *J. Geophys. Res.*, *114*, E08004, doi:10.1029/2008JE003277.

González-Galindo, F., J.-Y. Chaufray, M. A. López-Valverde, G. Gilli, F. Forget, F. Leblanc, R. Modolo, S. Hess, and M. Yagi (2013), Three-dimensional Martian ionosphere model: I. The photochemical ionosphere below 180 km, *J. Geophys. Res. Planets*, *118*, 2105–2123, doi:10.1002/jgre.20150.

Gurnett, D. A., et al. (2005), Radar soundings of the ionosphere of Mars, *Science*, *310*, 1929–1933, doi:10.1126/science.1121868.

Gurnett, D. A., et al. (2008), An overview of radar soundings of the Martian ionosphere from the Mars Express spacecraft, *Adv. Space Res.*, *41*, 1335–1346, doi:10.1016/j.asr.2007.01.062.

Hanson, W. B., and G. P. Mantas (1988), Viking electron temperature measurements—Evidence for a magnetic field in the Martian ionosphere, *J. Geophys. Res.*, *93*, 7538–7544, doi:10.1029/JA093iA07p07538.

Hanson, W. B., S. Sanatani, and D. R. Zuccaro (1977), The Martian ionosphere as observed by the Viking retarding potential analyzers, *J. Geophys. Res.*, *82*, 4351–4363, doi:10.1029/JS082i028p04351.

Knudsen, W. C., and K. L. Miller (1992), The Venus transterminator ion flux at solar maximum, *J. Geophys. Res.*, *97*, 17,165–17,167, doi:10.1029/92JA01460.

Knudsen, W. C., K. Spenner, K. L. Miller, and V. Novak (1980), Transport of ionospheric O^+ ions across the Venus terminator and implications, *J. Geophys. Res.*, *85*, 7803–7810, doi:10.1029/JA085iA13p07803.

Lillis, R. J., and D. A. Brain (2013), Nightside electron precipitation at Mars: Geographic variability and dependence on solar wind condition, *J. Geophys. Res. Space Physics*, *118*, 3546–3556, doi:10.1002/jgra50171.

Lillis, R. J., M. O. Fillingim, L. M. Peticolas, D. A. Brain, R. P. Lin, and S. W. Bougher (2009), Nightside ionosphere of Mars: Modeling the effects of crustal magnetic fields and electron pitch angle distributions on electron impact ionization, *J. Geophys. Res.*, *114*, E11009, doi:10.1029/2009JE003379.

Lillis, R. J., D. A. Brain, S. L. England, P. Withers, M. O. Fillingim, and A. Safaeinili (2010), Total electron content in the Mars ionosphere: Temporal studies and dependence on solar EUV flux, *J. Geophys. Res.*, *115*, A11314, doi:10.1029/2010JA015698.

Lundin, R., S. Barabash, A. Fedorov, H. Nilsson, J.-A. Sauvaud, and M. Yamauchi (2008a), Solar forcing and planetary ion escape from Mars, *Geophys. Res. Lett.*, *35*, L09203, doi:10.1029/2007GL032884.

Lundin, R., S. Barabash, M. Holmström, H. Nilsson, M. Yamauchi, M. Fraenz, and E. M. Dubini (2008b), A comet-like escape of ionospheric plasma from Mars, *Geophys. Res. Let.*, *35*, L18203, doi:10.1029/2008GL034811.

Ma, Y.-J., A. F. Nagy, K. C. Hansen, D. L. DeZeeuw, T. I. Gombosi, and K. G. Powell (2002), Three-dimensional multispecies MHD studies of the solar wind interaction with Mars in the presence of crustal fields, *J. Geophys. Res.*, *107*(A10), 1282, doi:10.1029/2002JA009293.

Ma, Y.-J., A. F. Nagy, I. V. Sokolov, and K. C. Hansen (2004), Three-dimensional, multispecies, high spatial resolution MHD studies of the solar wind interaction with Mars, *J. Geophys. Res.*, *109*, A07211, doi:10.1029/2003JA010367.

Matta, M., M. Galand, L. Moore, M. Mendillo, and P. Withers (2014), Numerical simulations of ion and electron temperatures in the ionosphere of Mars: Multiple ions and diurnal variations, *Icarus*, *227*, 78–88, doi:10.1016/j.icarus.2013.09.006.

McLain, J. L., V. Poterya, C. D. Molek, L. M. Babcock, and N. G. Adams (2004), Flowing afterglow studies of the temperature dependencies for dissociative recombination of O, CH, CH, CH with electrons, *J. Phys. Chem. A*, *108*, 6704–6708, doi:10.1021/jp040215l.

Miller, K. L., and R. C. Whitten (1991), Ion dynamics in the Venus ionosphere, *Space Sci. Rev.*, *55*, 165–199, doi:10.1007/BF00177137.

Mouginot, J., W. Kofman, A. Safaeinili, and A. Herique (2008), Correction of the ionospheric distortion on the MARSIS surface sounding echoes, *Planet. Space Sci.*, *56*, 917–926, doi:10.1016/j.pss.2008.01.010.

Morgan, D. D., D. A. Gurnett, D. L. Kirchner, J. L. Fox, E. Nielsen, and J. J. Plaut (2008), Variation of the Martian ionospheric electron density from Mars Express radar soundings, *J. Geophys. Res.*, *113*, A09303, doi:10.1029/2008JA013313.

Němec, F., D. D. Morgan, D. A. Gurnett, and F. Duru (2010), Nightside ionosphere of Mars: Radar soundings by the Mars Express spacecraft, *J. Geophys. Res.*, *115*, E12009, doi:10.1029/2010JE003663.

Němec, F., D. D. Morgan, D. A. Gurnett, F. Duru, and V. Truhlík (2011), Dayside ionosphere of Mars: Empirical model based on data from the MARSIS instrument, *J. Geophys. Res.*, *116*, E07003, doi:10.1029/2010JE003789.

Pätzold, M., S. Tellmann, B. Häusler, D. Hinson, R. Schaa, and G. L. Tyler (2005), A sporadic third layer in the ionosphere of Mars, *Science*, *310*, 837–839, doi:10.1126/science.1117755.

Pérez-de-Tejada, H. (1986a), Fluid dynamic constraints of the Venus ionospheric flow, *J. Geophys. Res.*, *91*, 6765–6770, doi:10.1029/JA091iA06p06765.

Pérez-de-Tejada, H. (1986b), Distribution of plasma and magnetic fluxes in the Venus near wake, *J. Geophys. Res.*, *91*, 8039–8044, doi:10.1029/JA091iA07p08039.

Pérez-de-Tejada, H. (1998), Momentum transport in the solar wind erosion of the Mars ionosphere, *J. Geophys. Res.*, *103*, 31,499–31,508, doi:10.1029/1998JE900001.

Pérez-de-Tejada, H. (2008), Asymmetry of the Venus nightside ionosphere: Magnus force effects, *Icarus*, *198*, 19–26, doi:10.1029/j.icarus.2008.05.025.

Pérez-de-Tejada, H., M. Dryer, and A. Badan-Dangon (1993), Comment on Plasma motion in the Venus ionosphere: Transition to supersonic flow" by R. C. Whitten, A. Barnes, and P. T. McCormick, *J. Geophys. Res.*, *98*, 17,485–17,487, doi:10.1029/93JA00723.

Pérez-de-Tejada, H., R. Lundin, H. Durand-Manterola, S. Barabash, T. L. Zhang, J. A. Sauvaud, and M. Reyes-Ruiz (2013), Solar wind-driven plasma fluxes from the Venus ionosphere, *J. Geophys. Res. Space Physics*, *118*, 7497–7506, doi:10.1002/2013JA019029.

Peverall, R., et al. (2001), Dissociative recombination and excitation of O_2^+: Cross sections, product yields and implications for studies of ionospheric airglows, *J. Chem. Phys.*, *114*, 6679–6689, doi:10.1063/1.1349079.

Picardi, G., et al. (2005), Radar soundings of the subsurface of Mars, *Science*, *310*, 1925–1928, doi:10.1126/science.1122165.

Rishbeth, H., and M. Mendillo (2004), Ionospheric layers of Mars and Earth, *Planet. Space Sci.*, *52*, 849–852, doi:10.1016/j.pss.2004.02.007.

Safaeinili, A., W. Kofman, J.-F. Nouvel, A. Herique, and R. L. Jordan (2003), Impact of Mars ionosphere on orbital radar sounder operation and data processing, *Planet. Space Sci.*, *51*, 505–515, doi:10.1016/S0032-0633(03)00048-5.

Safaeinili, A., W. Kofman, J. Mouginot, Y. Gim, A. Herique, A. B. Ivanov, J. J. Plaut, and G. Picardi (2007), Estimation of the total electron content of the Martian ionosphere using radar sounder surface echoes, *Geophys. Res. Lett.*, *34*, L23204, doi:10.1029/2007GL032154.

Spenner, K., W. C. Knudsen, R. C. Whitten, P. F. Michelson, K. L. Miller, and V. Novak (1981), On the maintenance of the Venus nightside ionosphere—Electron precipitation and plasma transport, *J. Geophys. Res.*, *86*, 9170–9178, doi:10.1029/JA086iA11p09170.

Ulusen, D., and I. Linscott (2008), Low-energy electron current in the Martian tail due to reconnection of draped interplanetary magnetic field and crustal magnetic fields, *J. Geophys. Res.*, *113*, E06001, doi:10.1029/2007JE002916.

Withers, P. (2009), A review of observed variability in the dayside ionosphere of Mars, *Adv. Space Res.*, *44*, 277–307, doi:10.1016/j.asr.2009.04.027.

Withers, P., M. O. Fillingim, R. J. Lillis, B. Häusler, D. P. Hinson, G. L. Tyler, M. Pätzold, K. Peter, S. Tellmann, and O. Witasse (2012), Observations of the nightside ionosphere of Mars by the Mars Express Radio Science Experiment (MaRS), *J. Geophys. Res.*, *117*, A12307, doi:10.1029/2012JA018185.

Withers, P., K. Fallows, and M. Matta (2014), Predictions of electron temperatures in the Mars ionosphere and their effects on electron densities, *Geophys. Res. Lett.*, *41*, 2681–2686, doi:10.1002/2014GL059683.

Whitten, R. C., A. Barnes, and P. T. McCormick (1991), Plasma motion in the Venus ionosphere—Transition to supersonic flow, *J. Geophys. Res.*, *96*, 11,057–11,064, doi:10.1029/91JA00318.

Zhang, M. H. G., J. G. Luhmann, and A. J. Kliore (1990), An observational study of the nightside ionospheres of Mars and Venus with radio occultation methods, *J. Geophys. Res.*, *95*, 17,095–17,102, doi:10.1029/JA095iA10p17095.